

Spacer Engineering Using Aromatic Formamidinium in 2D/3D Hybrid Perovskites for Highly Efficient Solar Cells

Tingting Liu,[‡] Jiahao Guo,[‡] Di Lu, Zhiyuan Xu, Qiang Fu, Nan Zheng, Zengqi Xie, Xiangjian Wan, Xiaodan Zhang, Yongsheng Liu,^{*} and Yongsheng Chen



Cite This: *ACS Nano* 2021, 15, 7811–7820



Read Online

ACCESS |



Metrics & More



Article Recommendations



Supporting Information

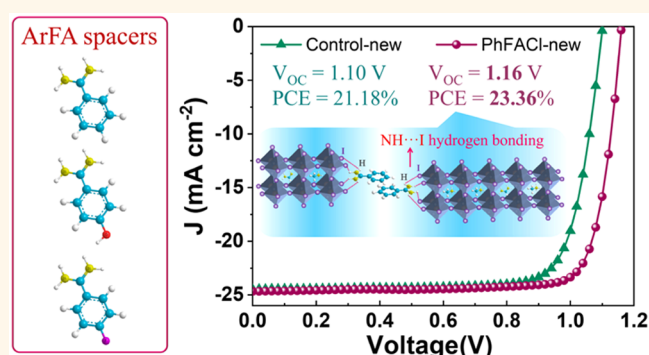
ABSTRACT: Organic spacers play an important role in 2D/3D hybrid perovskites, which could combine the advantages of high stability of 2D perovskites and high efficiency of 3D perovskites. Here, a class of aromatic formamidiniums (ArFA) was developed as spacers for 2D/3D perovskites. It is found that the bulky aromatic spacer ArFA in 2D/3D perovskites could induce better crystalline growth and orientation, reduce the defect states, and enlarge spatially resolved carrier lifetime thanks to the multiple NH \cdots I hydrogen-bonding interactions between ArFA and inorganic [PbI $_6$]⁴⁻ layers. As a result, compared to the control device with efficiency of 19.02%, the 2D/3D perovskite device based on such an optimized organic salt, namely benzamidinium hydrochloride (PhFACl), exhibits a dramatically improved efficiency of 22.39% along with improved long-term thermal stability under 80 °C over 1400 h. Importantly, a champion efficiency of 23.36% was further demonstrated through device engineering for PhFACl-based 2D/3D perovskite solar cells. These results indicate the great potential of this class of ArFA spacers in highly efficient 2D/3D perovskite solar cells.

KEYWORDS: organic spacer, perovskite solar cell, hydrogen-bonding interactions, spacer engineering, charge transport

INTRODUCTION

Metal halide perovskite solar cells (PSCs) are an emerging next-generation photovoltaic technology due to their dramatically increased power conversion efficiencies (PCEs) over the past decade.^{1–6} The impressive high PCEs are attributed to their unique optoelectronic properties, such as low exciton binding energy, long charge carrier lifetime, and high defect tolerance.^{7–9} However, the insufficient stability of the perovskite materials greatly hinders the commercialization of this technology.^{10,11}

Two-dimensional (2D) perovskites, such as 2D Ruddlesden–Popper (RP) and 2D Dion–Jacobson (DJ) structure perovskites, with bulky organic spacers have been developed to improve the intrinsic stability of perovskites due to their improved tolerance to moisture and thermal conditions.^{12–17} However, the PCEs of 2D perovskite devices are still much lower than their 3D counterparts owing to their larger exciton binding energy, lower carrier mobility, and wider bandgap.^{18–20} The incorporation of bulky organic spacers, which could prevent moisture invasion, improve thermal stability, and



suppress ion migration, into the 3D perovskite crystal lattice has been proven to be an effective strategy to combine the advantage of the high stability of 2D perovskite and the superior efficiency of 3D perovskite.^{21–26} Snaith *et al.* showed that 2D/3D PSCs with an optimal butylammonium content exhibit average stabilized power conversion efficiency of $17.5 \pm 1.3\%$ and the cells could sustain 80% of their “post burn-in” efficiency after 1000 h in air under simulated sunlight.²⁷ Huang *et al.* showed that the incorporation of the sulfonate zwitterion-based spacer could simultaneously control the perovskite crystallization and passivate defect states of perovskite films, which enhances the planar perovskite device efficiency to 21.1%, and the device retains 88% of the initial efficiency under

Received: March 13, 2021

Accepted: March 30, 2021

Published: April 2, 2021



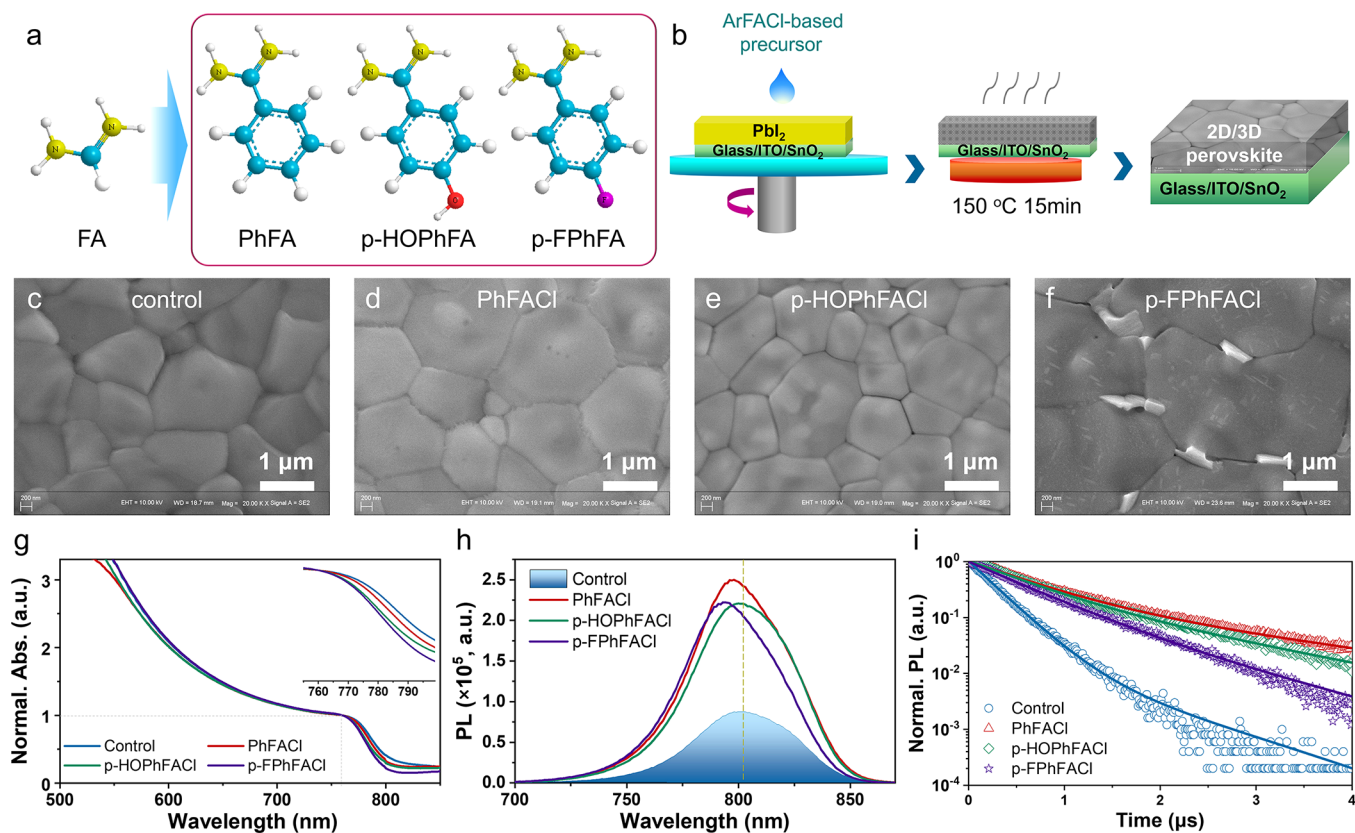


Figure 1. (a) Chemical structure of spacer cations FA, PhFA, *p*-HOPhFA, and *p*-FPhFA. (b) Procedures of preparation of 2D/3D perovskite films based on ArFACl. (c–f) Top view SEM images of perovskite films based on the control (c), PhFACl (d), *p*-HOPhFACl (e), and *p*-FPhFACl (f). (g–i) UV–vis absorption spectra (g), PL spectra (h), and TRPL spectra (i) of the control 3D and 2D/3D perovskite films.

continuous light illumination for 480 h.²⁸ However, the efficiencies of 2D/3D PSCs are still lower than that of state-of-the-art 3D PSCs. Thus, it is highly necessary to further develop more efficient organic spacers for 2D/3D PSCs and boost their efficiency for future industrial applications. Moreover, compared to methylammonium (MA), formamidinium (FA) has been widely studied and proven to be an excellent organic cation in 3D perovskites to reduce the bandgap and enhance the stability. Nevertheless, 2D/3D hybrid PSCs using FA-based derivatives as bulky spacers have rarely been reported.

In this work, a class of FA-based derivatives, namely aromatic formamidinium (ArFA), such as benzamidinium hydrochloride (PhFACl), 4-hydroxybenzamidinium hydrochloride (*p*-HOPhFACl) and 4-fluorobenzamidinium hydrochloride (*p*-FPhFACl), were developed for 2D/3D hybrid PSCs, and high photovoltaic performance has been demonstrated. By performing X-ray diffraction (XRD) and time-resolved photoluminescence (TRPL) experiments, we found that ArFA spacers have been successfully incorporated in the crystal lattice of the FA/MA-based 3D perovskite and form 2D/3D perovskite, leading to enhanced crystallinity, reduced trap density, and increased charge carrier lifetime. An enlarged PCE of 22.39% and stabilized PCE of 22.0% were achieved for PhFACl-based 2D/3D PSCs, coupled with an impressive open-circuit voltage (V_{OC}) of 1.16 V and a notable fill factor (FF) of 81.77%. Importantly, the PhFACl-based device exhibits high thermal stability, which sustains 87% of original performance after thermal aging test under 80 °C for 1480 h, while only ~66% of the initial efficiency remained for control 3D PSCs. Moreover, by further optimizing the perovskite film

with enlarged film thickness and improved film quality, the PhFACl-based 2D/3D device shows a champion efficiency of 23.36%, which is among the highest efficiency of 2D/3D hybrid PSCs. These results indicate that ArFA should be a class of excellent spacers for 2D/3D perovskite toward both highly efficient and stable solar cells.

RESULTS AND DISCUSSION

The 3D chemical structures of ArFA, including PhFA, *p*-HOPhFA, and *p*-FPhFA, are shown in Figure 1a. A sequential two-step deposition procedure was employed to fabricate 2D/3D perovskite films (Figure 1b). Briefly, a solution of PbI₂ in *N,N*-dimethylformamide (DMF) was spin-coated on the glass/ITO/SnO₂ substrate. After thermal annealing of the PbI₂ film, a mixed solution of FAI/MAI/MACl and ArFA spacers with optimized weight ratio in 2-propanol (IPA) was spin-coated on top of PbI₂ layer. Then the film was annealed at 150 °C for 15 min in air to form 2D/3D perovskites. Figure 1c–f displays the top-view scanning electron microscope (SEM) images of control 3D and 2D/3D perovskite films deposited on ITO/SnO₂ substrates. The corresponding grain size distributions are illustrated in Figure S1. Compared to the control 3D perovskite film, the 2D/3D perovskite films exhibit an average grain size over 1.4 μm, which is larger than that of the control 3D film, suggesting that the ArFA-based spacers could induce the crystal growth and improve the crystallinity of perovskite films. The large grain size of 2D/3D perovskite was in agreement with atomic force microscopy (AFM) images shown in Figure S2. The cross-section SEM images (Figure S3) further verify the enlarged grain size for 2D/3D

perovskites in comparison with the control 3D perovskite. The monolithic grains were observed growing between the top and bottom electrodes; thus, no obvious horizontal grain boundaries exist in the film, which facilitates the charge diffusion and transportation between two electrodes, leading to reduced nonradiative charge recombination.²⁹

Figure 1g shows the ultraviolet–visible (UV–vis) absorption spectra (normalized at 760 nm) of control and 2D/3D perovskite films. Compared with the control film, the 2D/3D perovskite films exhibit slightly blue-shifted onset absorption due to the incorporation of bulky ArFA spacers, such as PhFACl, *p*-HOPhFACl, and *p*-FPhFACl, leading to increased optical bandgap. The valence band maximum (VBM) of the perovskite films were measured by ultraviolet photoelectron spectroscopy (UPS) (Figure S4 and Table S1). Compared to the control film, the VBM of 2D/3D perovskite film shifted to lower band, which might be a feature of bandgap widening in the ArFA-based 2D/3D perovskite.^{30,31} The charge recombination kinetics in the control and 2D/3D perovskite films using nonconductive glass as substrates were analyzed through the photoluminescence (PL) and time-resolved photoluminescence (TRPL) spectra. As shown in Figure 1h, 2D/3D perovskite films based on PhFACl, *p*-HOPhFACl, and *p*-FPhFACl exhibit PL peaks at 798, 800, and 793 nm, respectively, which are slightly blue-shifted in comparison with the control film (803 nm) due to the interactions between ArFA spacers and the corner-sharing [PbI₆]⁴⁻ octahedron layers in 3D perovskite, which is consistent with the absorption spectra. Moreover, the PL intensity of 2D/3D perovskite was over 2 times higher compared to that of control 3D perovskite (Figure 1h), suggesting the reduced nonradiative recombination loss. The PL decay curves shown in Figure 1i were fitted through the following empirical biexponential dependence equation²⁸

$$y = A_1 \exp\left(\frac{-t}{\tau_1}\right) + A_2 \exp\left(\frac{-t}{\tau_2}\right) + B \quad (1)$$

where A_1 and A_2 are the relative amplitudes and τ_1 and τ_2 are the best-fit PL decay times for the fast and slow recombination.^{32,33} The average lifetime for the nonradiative recombination process and the specific data are calculated from the following equation^{33,34}

$$\tau_{\text{avg}} = \frac{\sum A_i \tau_i^2}{\sum A_i \tau_i} \quad (2)$$

The detailed data are summarized in Table S2. The calculated average lifetime of the control film is 421 ns, which is shorter than those of 1395, 1012, and 724 ns for perovskite films based on PhFACl, *p*-HOPhFACl, and *p*-FPhFACl, respectively. The longer charge carrier lifetime in 2D/3D perovskite suggest that the ArFA spacers could passivate the defect state and suppress the nonradiative recombination loss in the film, consistent with the lower trap density in the 2D/3D film as discussed below.

The iodide anions with electron rich lone-pair orbitals in corner-sharing [PbI₆]⁴⁻ octahedrons layers could accept hydrogen atoms from the ammonium fragment of organic spacers to form hydrogen bonds.^{35,36} As shown in Figure 2a, each ArFA spacer could form four NH...I hydrogen bonds. Thus, this might enhance the cohesion and chemically stabilize the 2D/3D perovskites efficiently, resulting in shifted X-ray diffraction (XRD) and X-ray photoelectron spectroscopy (XPS) peaks in comparison with control 3D perovskite as

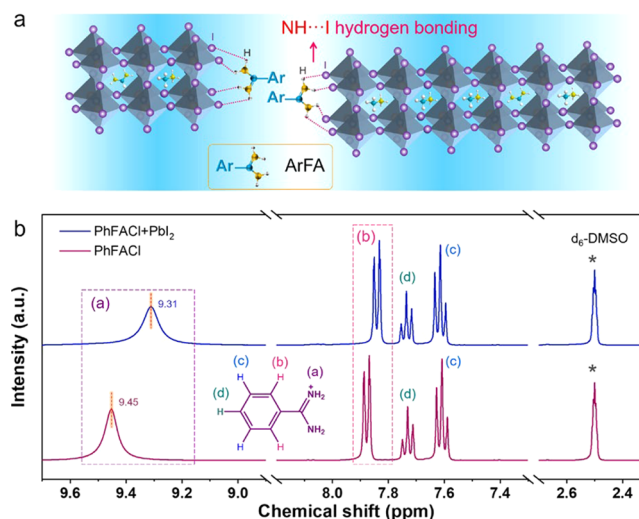


Figure 2. (a) Schematic diagram of corner-sharing [PbI₆]⁴⁻ octahedrons layers interaction with ArFA spacers through hydrogen bonding. (b) ¹H NMR spectra of pristine PhFACl and mixed PhFACl/PbI₂ showing changes in the resonance signals arising from the H protons.

discussed below.^{37–40} As a result, the incorporation of ArFA spacers enhances the perovskite grain size and crystallinity, consistent with SEM images above. The strong NH...I hydrogen-bonding interactions between organic spacer PhFA and inorganic [PbI₆]⁴⁻ octahedron layers were further verified by ¹H NMR spectral measurements as shown in Figure 2b. It is found that the proton signal of the –C(NH₂)₂⁺ groups in PhFACl appears at 9.45 ppm, which was shifted to 9.31 ppm when blended with PbI₂, suggesting the strong NH...I hydrogen-bonding interactions. Note that there is an obvious shift for the protons in the benzene ring of PhFACl close to the FA cation shown in Figure 2b due to the different chemical environment caused by electronic cloud distribution after NH...I hydrogen bonding.

The XRD patterns of the perovskite films prepared on the compact glass/ITO/SnO₂ substrate are shown in Figure 3a, and enlarged peaks between 13.5° and 15° are shown in Figure 3b. The diffraction peaks at 14.26° and 28.46° correspond to (110) and (220) lattice planes of the control 3D perovskite film, respectively. As shown in Figure 3b for the magnified plot of the (110) diffraction peaks, there is an obvious shift toward lower angles for ArFA-based perovskite films in comparison with control film due to the enlarged *d*-spacing and lattice distortion. The results indicate that there are strong hydrogen-bonding interactions between the ArFA and inorganic [PbI₆]⁴⁻ layers, and ArFA spacers have been inserted into the 3D perovskite film and form 2D/3D hybrid perovskite, which was further confirmed by the TEM results discussed below. The dramatically increased diffraction peak intensity of 2D/3D perovskites suggest that the crystallinity of perovskites was significantly improved after the incorporation of different ArFA spacers. Note that the PhFACl-based film shows stronger (110) diffraction peak intensity and narrower full width at half maxima (fwhm) (Figure S5) compared to other ArFA-based films, consistent with its best crystallinity for this series of 2D/3D perovskite as shown in the SEM images above.

Figure 3c,d and Figure S6 show the XPS patterns of control 3D and 2D/3D perovskite films. Compared to the control film, the Pb 4f and I 3d peaks in the XPS spectra of 2D/3D films

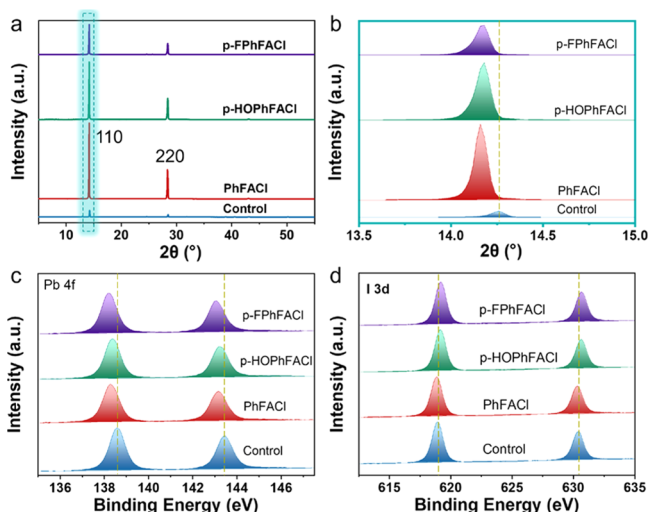


Figure 3. (a) XRD patterns of the control 3D perovskite film and the 2D/3D perovskite films based on PhFACI, *p*-HOPhFACI and *p*-FPhFACI. (b) Enlarged plot of the (110) diffraction peaks of XRD patterns of corresponding perovskite films. (c) XPS spectra of Pb 4f for control 3D perovskite and 2D/3D perovskite films. (d) XPS spectra of I 3d for control 3D perovskite and 2D/3D perovskite films.

exhibit obvious shifts, suggesting the changed chemical bonding of the Pb and I atoms after incorporation of ArFAX. The ArFA is an organic cation that could not interact with the uncoordinated Pb^{2+} cations and passivate the Pb defect. The shift in I 3d after incorporating ArFA could be ascribed to the $\text{NH}\cdots\text{I}$ hydrogen interaction. Note that each ArFA could form four $\text{NH}\cdots\text{I}$ hydrogen bonds, which could have direct effects on the Pb–I bond length, resulting shifted binding energy in Pb 4f. These results are in good agreement with the XRD results, further validating that the ArFA have been embedded in the perovskite crystal lattice and form the 2D/3D perovskites.

The control 3D and ArFA spacer-based 2D/3D PSCs with planar n-i-p architecture were investigated under standard simulated AM 1.5G 100 mW cm^{-2} illumination (Figure S7), and the detailed parameters are summarized in Table 1. The statistical photovoltaic parameters for the control device and 2D/3D perovskite devices based on PhFACI, *p*-HOPhFACI, and *p*-FPhFACI are shown in Figure 4a,b. The control device achieved an average PCE of 18.35%, while the average PCE was improved to 21.42%, 20.90%, and 20.65% for PhFACI-, *p*-HOPhFACI-, and *p*-FPhFACI-based 2D/3D perovskite devices, respectively. V_{OC} tends to increase from an average V_{OC} of 1.06 V for the control device to 1.15 V for PhFACI-, *p*-HOPhFACI-, and *p*-FPhFACI-based devices. The FF is obviously improved after incorporating ArFA spacers in 3D perovskites with average FF increased from 78.6% to 80.8%.

Table 1. Optimized Photovoltaic Device Parameters Based on Control 3D Perovskite and 2D/3D Perovskites Using Different Aromatic Amidinium Spacers

material	V_{OC} (V)	J_{SC} (mA cm^{-2})	J_{SC}^a (mA cm^{-2})	FF (%)	PCE _{best} /PCE _{average} (%)	V_{TFL} (V)	N_{t}^{hb} (cm^{-3})
control	1.06	22.28	22.64	80.25	19.02/18.36	0.42	1.85×10^{15}
PhFACI	1.16	23.60	23.37	81.77	22.39/21.41	0.22	9.70×10^{14}
<i>p</i> -HOFACI	1.16	23.21	22.44	81.89	22.05/20.90	0.21	9.26×10^{14}
<i>p</i> -FPhFACI	1.16	23.24	22.90	81.73	22.03/20.63	0.26	1.15×10^{15}

^aIntegrated JSC from EQE data. ^bTrap density calculated from hole-only device.

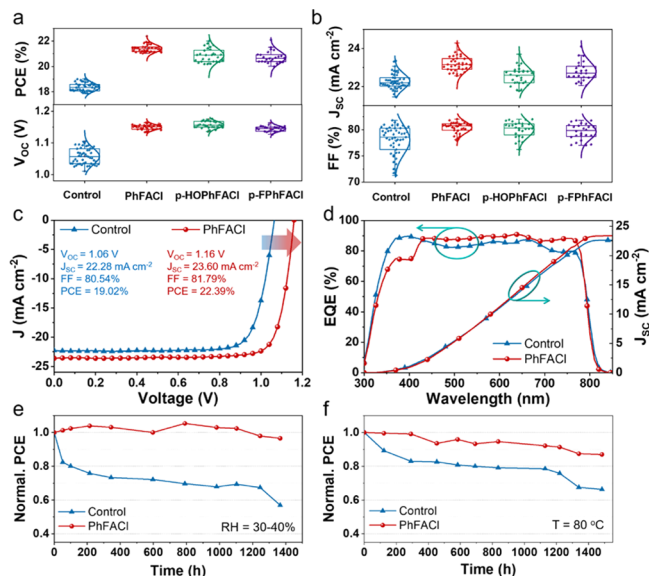


Figure 4. (a) Statistical data for PCE and V_{OC} obtained from 24 devices for control and 2D/3D PSCs. (b) Statistical data for J_{SC} and FF obtained from 24 devices for control and 2D/3D PSCs. (c) J – V curves of the devices based on control 3D and 2D/3D perovskites. (d) EQE spectra with integrated J_{SC} of the corresponding devices. (e) Long-term stability of devices storage in air (RH = 30–40%). (f) Thermal stability testing of PSCs under 80 °C in N₂ glovebox.

The significantly enhanced V_{OC} and FF could be attributed to their enhanced crystallinity, reduced trap density, and enlarged carrier lifetime as discussed below. The PhFACI-based 2D/3D perovskite devices exhibit very narrow distribution of PCEs, suggesting their better reproducibility in comparison with control devices. As shown in Figure 4c, the control device exhibits a PCE of 19.02%, a short-circuit current density (J_{SC}) of 22.28 mA cm^{-2} , a V_{OC} of 1.06 V, and an FF of 80.25%. A champion efficiency of 22.39% was achieved for the PhFACI-based device, combined with a J_{SC} of 23.60 mA cm^{-2} , a large V_{OC} of 1.16 V, and a notable FF of 81.77%. Moreover, the PSCs based on *p*-HOPhFACI or *p*-FPhFACI also exhibit improved PCE of over 22%, impressive V_{OC} of 1.16 V, and notable FF closed to 82%, as illustrated in Figure S7 and Table 1. Based on the morphology, XPS, and other results discussed above, we argue that the main driving force for the improved crystallinity and PCEs might be the existence of the multiple hydrogen-bonding interactions between the ArFA spacers and inorganic $[\text{PbI}_6]^{4-}$ layer. Note that the ArFA-based devices show hysteresis, which is similar to the previously reported 2D/3D perovskite devices (Figure S8).^{41,42} The integrated J_{SC} extracted from external quantum efficiency (EQE) (Figure 4d) spectra are 22.64 and 23.37 mA cm^{-2} for the control and PhFACI-based devices, respectively, consistent with the values

measured from J - V curves. The steady-state efficiencies of the devices by holding the voltage of at max power point (MPP) are shown in Figure S7c, in good agreement with the J - V results.

The aging test was studied to evaluate the effect of ArFA spacers on the stability of the PSCs (Figure 4e,f, Figure S9–S11). Note that we employ gold (Au) to replace silver (Ag) as the top electrode for the device stability test. As shown in Figure 4e, the control devices decayed to lower than 56% of its original PCEs after 1360 h, while the PhFACI-incorporated 2D/3D hybrid PSCs still retained \sim 95% of its initial PCEs under ambient atmosphere with relative humidity (RH) of 30–40%, suggesting bulky PhFA spacers could also more efficiently block the moisture invasion and improve the humidity stability of the devices. The thermal aging tests of unencapsulated devices at 80 °C are shown in Figure 4f. The PhFACI-based 2D/3D hybrid PSCs could maintain 87% of its initial efficiency after 1480 h (over 61 days). On the contrary, the PCEs of the control device showed obvious degradation with a loss of 34% of the initial value. Furthermore, the ArFA spacers incorporated 2D/3D hybrid PSCs could sustain over 99% of initial efficiency after storage in N₂ glovebox for 2500 h (over 104 days), while the control devices dropped to \sim 77% of its original PCEs (Figure S11). The significantly improved stability and maintained high efficiency indicate the great potential of these ArFA spacers developed in this work for efficient and stable 2D/3D PSCs.

The light intensity dependence of V_{OC} was investigated to understand the charge recombination kinetics within the devices.²⁹ Figure 5a shows the seminatural logarithmic plot of

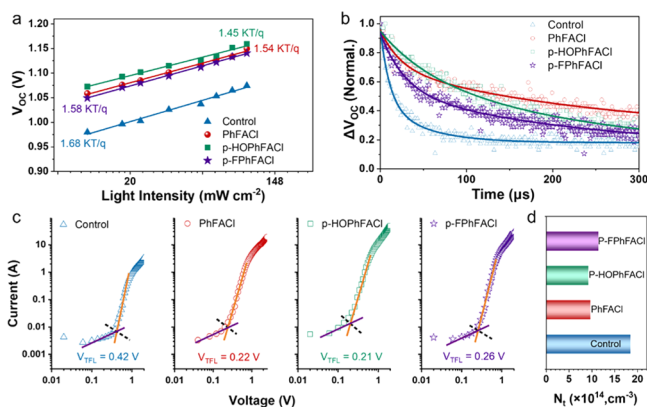


Figure 5. (a) V_{OC} as a function of light intensity for control device and 2D/3D perovskite devices based on PhFACI, *p*-HOPhFACI, and *p*-FPhFACI. (b) Transient photovoltage decay curves of the corresponding devices. (c) I - V curves of the hole-only SCLC devices based on control and 2D/3D perovskites. (d) Extracted defects density (N_t) for the corresponding perovskite films.

V_{OC} as a function of light intensity for the control and 2D/3D perovskite devices. The slopes derived from the lines fitted linearly to the data are 1.54, 1.45, and 1.58 kT/q for devices based on PhFACI, *p*-HOPhFACI, and *p*-FPhFACI, respectively, which are lower than that of the control device (1.68 kT/q), indicating the suppressed trap-assisted Shockley–Read–Hall (SRH) recombination due to the improved crystallinity and hindered ions migration in 2D/3D perovskites.^{19–21} To gain more profound comprehension of the carrier dynamics, we carried out transient photovoltage (TPV) and transient photocurrent (TPC) measurements of the control and 2D/

3D PSCs. As shown in Figure 5b, the photovoltage decay time of 2D/3D devices based on PhFACI, *p*-HOPhFACI, and *p*-FPhFACI are 198.5, 158.0, and 158.5 μs , respectively, which are much larger than that of the control device (49.1 μs). The prolonged decay time suggested the enlarged charge carrier lifetimes and reduced carrier recombination rate in ArFA-based 2D/3D PSCs, which could be ascribed to the lower defect density in the film as discussed above. The TPC curves (Figure S12) show that PhFACI-, *p*-HOPhFACI-, and *p*-FPhFACI-based devices exhibit decay times of 1.9, 2.0, and 2.3 μs , respectively, which are shorter than that of the control device (3.2 μs), suggesting the enhanced charge extraction efficiency and reduced interfacial charge accumulation and recombination.⁴³ The increased charge carrier lifetime and improved charge extraction efficiency for 2D/3D perovskite devices could result in improved V_{OC} and FF, consistent with the photovoltaic performance discussed above.

The trap-state density of the perovskite films was calculated by performing the space-charge-limited current (SCLC) measurements, and detailed data are summarized in Table 1.⁴⁴ Figure 5c displays the I - V characteristics in the dark of the control and 2D/3D perovskite films. At low bias voltage, the linear region could be assigned to the ohmic response ($I \propto V = 1$), and the intermediate region is the trap-filling process ($I \propto V > 3$).⁴⁵ The trap-filled limit voltage (V_{TFL}) is the kink point of the two different regions (Figure 5c). The trap density (N_t) and the V_{TFL} follow the equation^{46,47} $N_t = (2\epsilon\epsilon_0 V_{TFL}) / (eL^2)$, where ϵ is the relative dielectric constant of perovskite (\sim 32),⁴⁶ ϵ_0 is the vacuum dielectric permittivity, e is the elementary charge, and L is the thickness of perovskite film. The N_t were estimated to be 9.70×10^{14} , 9.26×10^{14} , and $1.15 \times 10^{15} \text{ cm}^{-3}$ for the 2D/3D films based on PhFACI, *p*-HOPhFACI, and *p*-FPhFACI, respectively. The reduced trap density for 2D/3D films in comparison with control film ($1.85 \times 10^{15} \text{ cm}^{-3}$) could be attributed to their superior film quality with increased crystallinity and hindered ion migration after the incorporation of bulky ArFA spacers.

To reveal the inner structure property and verify the existence of both 2D RP and 3D phases in ArFA-based perovskite films, we conducted high-resolution transmission electron microscope (HRTEM) measurements. As shown in Figure 6a–c, the HRTEM images clearly show polycrystalline grains with large crystalline interplanar spacing, which are corresponding to fingerprint of 2D lattice fringes and are analyzed with fast Fourier transform (FFT) analysis. The spot diffraction of control 3D perovskite film (Figure S13) exhibits interplanar distance of 3.2 Å, which agrees well with the representative (220) diffraction of the control 3D perovskite.⁴⁸ The TEM and FFT analysis images show that different interplanar distance coexist in the PhFACI-based 2D/3D hybrid perovskite film including the distance of 3.2 and 6.7 Å, which correspond to the 3D perovskite phase (Figure S13) and layered 2D RP perovskite phase, respectively.⁴⁸ The formed 2D phase was further confirmed by the XRD pattern of pure 2D perovskite (PhFA)₂PbI₄ (Figure S14 and Table S3), which exhibits a (006) diffraction peak, corresponding to a d -spacing 6.7 Å, in good agreement of TEM results. As shown in Figure 6b,c, the *p*-HOPhFACI- and *p*-FPhFACI-based 2D/3D perovskite films also exhibit the interplanar distance of 3.2 Å, indicating the presence of 3D perovskite phases, and the interplanar distance of 7.1 and 7.6 Å correlating with the layered 2D RP perovskite phases.^{48,49} These results clearly show that the 2D RP perovskite phases and 3D phases coexist

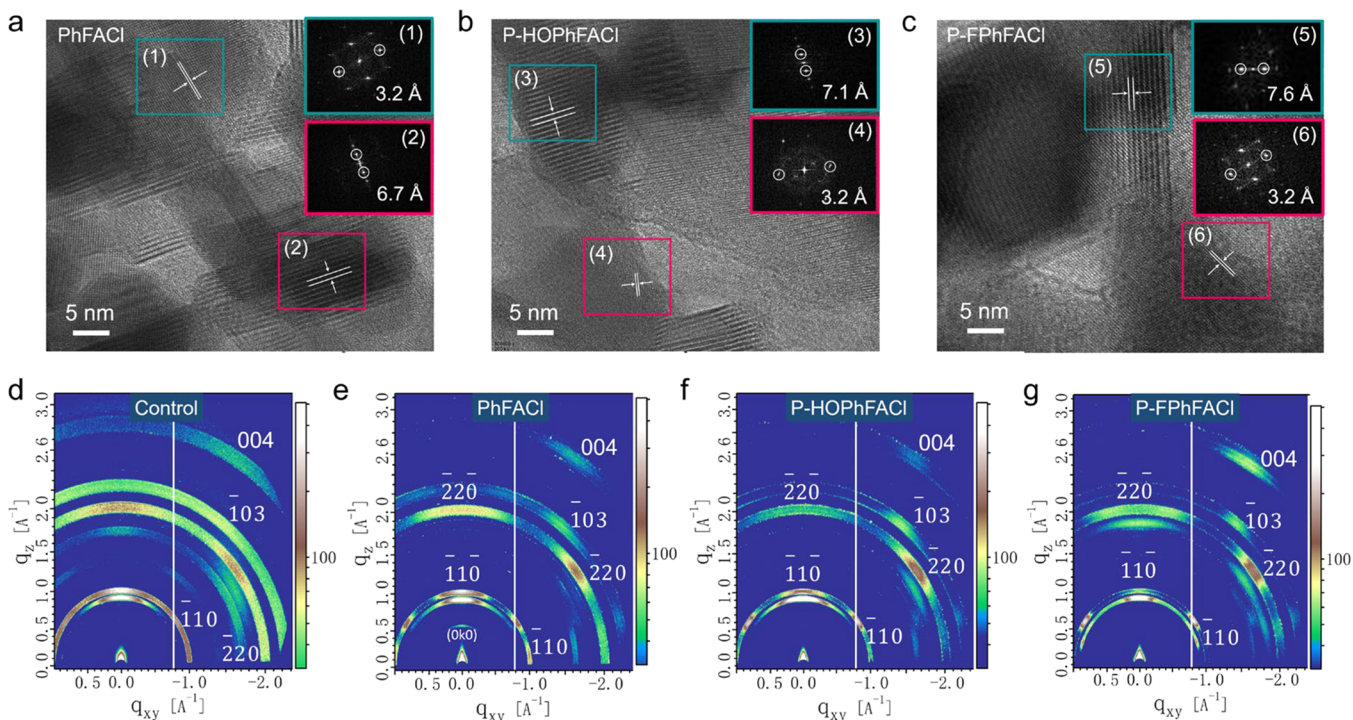


Figure 6. (a–c) HRTEM of the 2D/3D hybrid perovskite films based on PhFACI (a), *p*-HOPhFACI (b), and *p*-FPhFACI (c). Insets of a–c show FFT analysis images of the area within boxes. (d–g) GIWAXS patterns of the control (d), PhFACI (e), *p*-HOPhFACI (f), and *p*-FPhFACI (g) based perovskite films.

and distributed randomly in the ArFA-based 2D/3D hybrid perovskite films matched well with the improved stability due to the incorporation of ArFA-based spacers in the crystal lattice discussed above. Note that the TEM gives the same interplanar distance (3.2 Å) among 3D and 2D/3D samples, whereas the XRD of 2D/3D samples showed the shifted (110) diffraction peaks and slightly enlarged *d*-spacing in comparison with 3D control film. This is because, compared to control 3D perovskite, the shifting of *d*-spacing of (110) plane for 2D/3D perovskite films is only about 0.04 Å (Table S4), which is too small to be distinguished in TEM images.

To further investigate the crystallographic quality and orientation of the perovskite crystal in the films, the grazing-incidence wide-angle X-ray scattering (GIWAXS) measurement was performed for the control and 2D/3D perovskite films (Figure 6d–g). The control film exhibits broad Debye–Scherrer diffraction rings, which are the key features of the 3D perovskite structure, suggesting the isotropic crystal orientation distribution of the perovskite crystals.⁵⁰ In contrast, for the ArFA-based 2D/3D perovskite, the diffraction rings partially disappeared and turned into sharp and distinct Bragg spots, which suggests partial reorientation of the crystal with preferred vertical orientation with respect to the substrate due to the incorporation of ArFA spacers, and thus, the preferentially orientated 2D/3D hybrid perovskites were formed.²⁷ Note that Figure 6e shows a Bragg dot in the small *q*-value region, which exhibits larger *d*-spacing than that of 3D perovskite and could be assigned to (0*k*0) crystallographic planes of 2D perovskite in sample containing PhFA spacer.^{26,27}

To elucidate the spatially resolved carrier lifetime and PL intensity distribution in PhFACI-based 2D/3D perovskite films, we performed time-resolved confocal fluorescence microscopy (TCFM). The TCFM of the control 3D perovskite

film was also measured for comparison. The PL intensity map and *in situ* spatially resolved PL lifetime map are shown in the same image using gray and color scales, respectively. As shown in Figure 7a,b, the obvious spatial heterogeneity in PL intensity can be observed for both films due to the spatial variation in the distribution of trap states. Compared to the control film with a dark blue color in the TCFM image, the target film displays bright green color and obvious crystal grains, which is

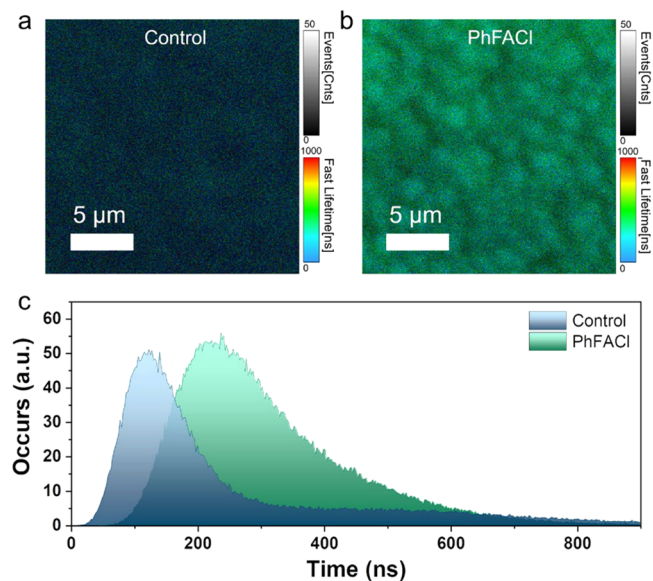


Figure 7. Time-resolved confocal fluorescence microscopy images of the control (a) and PhFACI-based 2D/3D perovskite films (b). (c) PL occurs distribution of different carrier lifetime for the corresponding films.

ascribed to the different trap density in bulk crystal and grain boundary, suggesting its overall enhanced PL intensity and spatially resolved longer carrier lifetime. The corresponding PL of the corresponding TCFM images in Figure 7c shows carrier lifetime distribution in the perovskite films, where the control film exhibits narrow full width at half-maximum (fwhm) of 118 ns and a peak at 122 ns. In contrast, the 2D/3D perovskite film exhibits a wider fwhm of 229 ns and a peak at 221 ns, suggesting its longer average carrier lifetime in the whole perovskite film. The spatial distribution of PL counts further indicates a higher charge carrier concentration and longer average carrier lifetime, in agreement with PL and TPRL spectra results discussed above, suggesting the reduced trap density and suppressed charge carrier nonradiative recombination loss.

Given the obviously improved V_{OC} and FF of the PhFACI-based 2D/3D perovskite device, we believe the efficiency could be further improved by increasing the J_{SC} of the devices. Thus, we further optimized the control device, namely control-new device, by increasing the film thickness (from ~ 437 to ~ 642 nm, Figures S3 and S15) with optimized morphology to harvest more solar light. As shown in Figure 8a, the control-

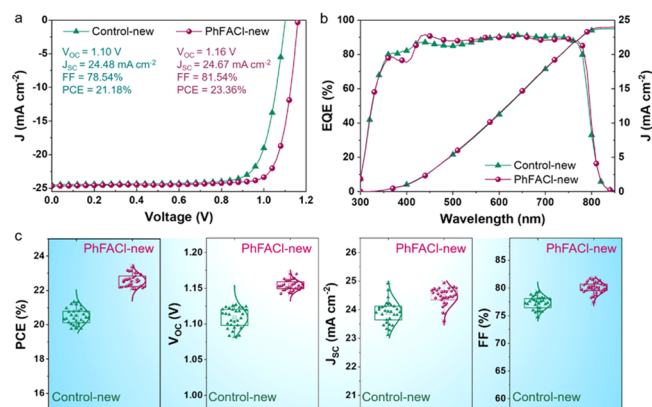


Figure 8. (a) J - V curves of the devices based on control-new 3D and PhFACI-new 2D/3D perovskites. (b) EQE spectra with integrated J_{SC} of corresponding devices. (c) The distribution of the photovoltaic characteristics of control-new devices and PhFACI-new based 2D/3D hybrid perovskite devices (30 individual devices were collected).

new device shows an enlarged PCE of 21.18%, combined with an obviously increased J_{SC} of 24.48 mA cm $^{-2}$, a V_{OC} of 1.10 V, and an FF of 78.54%. Using a similar film fabrication procedure of control-new perovskite, the PhFACI-based 2D/3D device shows a high J_{SC} of 24.67 mA cm $^{-2}$, an increased V_{OC} of 1.16 V, and a notable FF of 81.54%, yielding a champion PCE as high as 23.36%. The increased J_{SC} of control-new or PhFACI-based 2D/3D devices are consistent with the optimized film thickness of perovskite film as shown in Figure S15 for the corresponding cross-section SEM images. Note that the devices show hysteresis under different scanning conditions (Figure S16, Table S5), similar to previous reports.^{51–54} Importantly, as shown in Figure 8c, the PhFACI-based 2D/3D PSCs show excellent reproducibility with an average PCE of 22.56%, much higher than that of control-new devices (PCE_{average} = 20.46%). The detailed statistical photovoltaic performance parameters as a function of PhFACI concentration of the devices are shown in Figure

S17. These results further suggest the great potential of ArFA spacers for highly efficient perovskite solar cells.

CONCLUSIONS

In summary, we have developed a class of aromatic amidinium halides, such as PhFACI, *p*-HOPhFACI, and *p*-FPhFACI, for 2D/3D hybrid perovskites, and highly efficient and stable solar cells have been successfully demonstrated through the spacer engineering strategy. It is found that the incorporation of bulky ArFA spacers in perovskites could induce better crystal growth and orientation and reduce trap density, leading to increased carrier lifetime and suppressed charge carrier nonradiative recombination loss, possibly due to the strong hydrogen bonding interactions between ArFA and inorganic [PbI₆]⁴⁻ layers. Compared to the control device ($V_{OC} = 1.06$ V, PCE = 19.02%), the 2D/3D PSCs based on ArFACI (PhFACI, *p*-HOPhFACI, and *p*-FPhFACI) all showed a significantly enhanced V_{OC} of 1.16 V and high PCEs over 22%, with champion efficiency of 22.39% for PhFACI-based devices. Importantly, the 2D/3D PSCs also exhibit dramatically enhanced device stability. For example, the unencapsulated ArFA-based devices sustained 87% of their initial PCEs after thermal aging test under 80 °C for 1480 h, while only $\sim 66\%$ of the initial efficiency remained for the control device. Importantly, a champion efficiency of 23.36% was further achieved by optimizing the photovoltaic layer with enlarged film thickness and improved film quality. Our results indicate that ArFA spacers might be a class of excellent spacer candidates for highly efficient 2D/3D PSCs.

EXPERIMENTAL SECTION

Perovskite Precursor Preparation. PbI₂ was dissolved in DMF/DMSO (95:5) at a concentration of 1.2 M. For the control organic salt solution, FAI, MAI, and MACI were mixed and dissolved in 2-propanol with a concentration of 51, 9, and 12 mg mL $^{-1}$, respectively. For the ArFACI (such as PhFACI, *p*-HOPhFACI, and *p*-FPhFACI) incorporated organic salt precursor solution, ArFACI was dissolved in the control organic salt solution with a concentration of 2 mg mL $^{-1}$. The Spiro-OMeTAD solution was prepared with a concentration of 80 mg mL $^{-1}$ in chlorobenzene, in which 30 μ L of 4-*tert*-butylpyridine and 35 μ L of lithium bis(trifluoromethylsulfonyl)imide (260 mg mL $^{-1}$ in acetonitrile) were added as additives. For thick perovskite film based control-new film, PbI₂ was dissolved in DMF/DMSO (94:6) at a concentration of 1.5 M. For the control-new organic salt solution, FAI, MAI, and MACI were mixed and dissolved in 2-propanol with a concentration of 76.5, 13.5, and 18 mg mL $^{-1}$, respectively. For the PhFACI-incorporated organic salt new precursor solution (PhFACI-new), PhFACI was dissolved in the control organic salt solution with a concentration of 3.5 mg mL $^{-1}$.

Device Fabrication. The ITO substrate was sequentially washed with distilled water, acetone, and 2-propanol. A thin layer of SnO₂ was spin-coated onto ITO substrate at 3000 rpm for 30 s in ambient air. After being annealed at 150 °C for 30 min, the substrates were transferred into an N₂-filled glovebox. Then the PbI₂ solution was deposited by spin coating at 1500 rpm for 30 s and dried at 70 °C for 1 min. After being cooled to room temperature, the control (FAI/MAI/MACI) or ArFACI-incorporated (FAI/MAI/MACI/ArFACI) organic salt solution was spin-coated on the top of the PbI₂ layer at 1700 rpm for 40 s, followed by thermal annealing at 150 °C for 15 min in air. For control-new and PhFACI-new perovskite films, the PbI₂ solution (1.5 M) was deposited by spin coating at 1800 rpm for 30 s and then dried at 70 °C for 1 min. After being cooled to room temperature, the control-new (FAI/MAI/MACI) or ArFACI-new (FAI/MAI/MACI/PhFACI) organic salt solution was spin-coated on top of the PbI₂ layer at 2300 rpm for 40 s, followed by thermal annealing at 160 °C for 15 min in air. The Spiro-OMeTAD solution

was then spin coated onto the perovskite layer at 6000 rpm for 30 s. The as-deposited samples were aged under dry air conditions for ~12 h. Finally, a 15 nm MoO₃ layer and 80 nm Ag layer were deposited by thermal evaporation under a pressure of $\sim 1.0 \times 10^{-4}$ Pa. The effective area of each cell was 0.1 cm² as defined by mask.

ASSOCIATED CONTENT

Supporting Information

The Supporting Information is available free of charge at <https://pubs.acs.org/doi/10.1021/acsnano.1c02191>.

Further information on materials and characterization details; UPS spectra; AFM, SEM, and XRD; additional J–V and stability data (PDF)

AUTHOR INFORMATION

Corresponding Author

Yongsheng Liu – *The Centre of Nanoscale Science and Technology and Key Laboratory of Functional Polymer Materials, Institute of Polymer Chemistry, College of Chemistry, Nankai University, Tianjin 300071, China; Renewable Energy Conversion and Storage Center (RECAST), Nankai University, Tianjin 300071, China;* orcid.org/0000-0002-7135-723X; Email: liuys@nankai.edu.cn

Authors

Tingting Liu – *The Centre of Nanoscale Science and Technology and Key Laboratory of Functional Polymer Materials, Institute of Polymer Chemistry, College of Chemistry, Nankai University, Tianjin 300071, China*

Jiahao Guo – *The Centre of Nanoscale Science and Technology and Key Laboratory of Functional Polymer Materials, Institute of Polymer Chemistry, College of Chemistry, Nankai University, Tianjin 300071, China*

Di Lu – *The Centre of Nanoscale Science and Technology and Key Laboratory of Functional Polymer Materials, Institute of Polymer Chemistry, College of Chemistry, Nankai University, Tianjin 300071, China*

Zhiyuan Xu – *The Centre of Nanoscale Science and Technology and Key Laboratory of Functional Polymer Materials, Institute of Polymer Chemistry, College of Chemistry, Nankai University, Tianjin 300071, China*

Qiang Fu – *The Centre of Nanoscale Science and Technology and Key Laboratory of Functional Polymer Materials, Institute of Polymer Chemistry, College of Chemistry, Nankai University, Tianjin 300071, China*

Nan Zheng – *Institute of Polymer Optoelectronic Materials and Devices, State Key Laboratory of Luminescent Materials and Devices, South China University of Technology, Guangzhou 510640, China*

Zengqi Xie – *Institute of Polymer Optoelectronic Materials and Devices, State Key Laboratory of Luminescent Materials and Devices, South China University of Technology, Guangzhou 510640, China;* orcid.org/0000-0002-9805-8176

Xiangjian Wan – *The Centre of Nanoscale Science and Technology and Key Laboratory of Functional Polymer Materials, Institute of Polymer Chemistry, College of Chemistry, Nankai University, Tianjin 300071, China; Renewable Energy Conversion and Storage Center (RECAST), Nankai University, Tianjin 300071, China*

Xiaodan Zhang – *Institute of Photoelectronic Thin Film Devices and Technology, Nankai University, Tianjin 300071,*

China; Renewable Energy Conversion and Storage Center (RECAST), Nankai University, Tianjin 300071, China; orcid.org/0000-0002-0522-5052

Yongsheng Chen – *The Centre of Nanoscale Science and Technology and Key Laboratory of Functional Polymer Materials, Institute of Polymer Chemistry, College of Chemistry, Nankai University, Tianjin 300071, China; Renewable Energy Conversion and Storage Center (RECAST), Nankai University, Tianjin 300071, China;* orcid.org/0000-0003-1448-8177

Complete contact information is available at: <https://pubs.acs.org/doi/10.1021/acsnano.1c02191>

Author Contributions

[‡]T.L. and J.G. contributed equally.

Notes

The authors declare no competing financial interest.

ACKNOWLEDGMENTS

The authors gratefully acknowledge the financial support from the National Natural Science Foundation of China (Grant Nos. 21875122 and 51673097), MoST of China (Grant No. 2019YFA0705900), and 100 Young-Academic-Leader Team Program of Nankai University (Grant No. 075-63201171).

REFERENCES

- (1) Kim, H.-S.; Lee, C.-R.; Im, J.-H.; Lee, K.-B.; Moehl, T.; Marchioro, A.; Moon, S.-J.; Humphry-Baker, R.; Yum, J.-H.; Moser, J. E.; Grätzel, M.; Park, N.-G. Lead Iodide Perovskite Sensitized All-Solid-State Submicron Thin Film Mesoscopic Solar Cell with Efficiency Exceeding 9%. *Sci. Rep.* **2012**, *2*, 590–591.
- (2) Min, H.; Kim, M.; Lee, S. U.; Kim, H.; Kim, G.; Choi, K.; Lee, J. H.; Seok, S. I. Efficient, Stable Solar Cells by Using Inherent Bandgap of Alpha-Phase Formamidinium Lead Iodide. *Science* **2019**, *366*, 749–753.
- (3) Kojima, A.; Teshima, K.; Shirai, Y.; Miyasaka, T. Organometal Halide Perovskites as Visible-Light Sensitizers for Photovoltaic Cells. *J. Am. Chem. Soc.* **2009**, *131*, 6050–6051.
- (4) Jiang, Q.; Zhao, Y.; Zhang, X. W.; Yang, X. L.; Chen, Y.; Chu, Z. M.; Ye, Q. F.; Li, X. X.; Yin, Z. G.; You, J. B. Surface Passivation of Perovskite Film for Efficient Solar Cells. *Nat. Photonics* **2019**, *13*, 500–501.
- (5) Zhu, H. W.; Liu, Y. H.; Eickemeyer, F. T.; Pan, L. F.; Ren, D.; Ruiz-Preciado, M. A.; Carlsen, B.; Yang, B. W.; Dong, X. F.; Wang, Z. W.; Liu, H. L.; Wang, S. R.; Zakeeruddin, S. M.; Hagfeldt, A.; Dar, M. I.; Li, X. G.; Grätzel, M. Tailored Amphiphilic Molecular Mitigators for Stable Perovskite Solar Cells with 23.5% Efficiency. *Adv. Mater.* **2020**, *32*, 1907757.
- (6) National Renewable Energy Laboratory Efficiency Chart, <https://www.nrel.gov/pv/cell-efficiency.html> (accessed January 2021).
- (7) Jena, A. K.; Kulkarni, A.; Miyasaka, T. Halide Perovskite Photovoltaics: Background, Status, and Future Prospects. *Chem. Rev.* **2019**, *119*, 3036–3103.
- (8) Fu, Y. P.; Zhu, H. M.; Chen, J.; Hautzinger, M. P.; Zhu, X. Y.; Jin, S. Metal Halide Perovskite Nanostructures for Optoelectronic Applications and the Study of Physical Properties. *Nat. Rev. Mater.* **2019**, *4*, 169–188.
- (9) Huang, J.; Yuan, Y.; Shao, Y.; Yan, Y. Understanding the Physical Properties of Hybrid Perovskites for Photovoltaic Applications. *Nat. Rev. Mater.* **2017**, *2*, 17042.
- (10) Park, B. W.; Seok, S. I. Intrinsic Instability of Inorganic–Organic Hybrid Halide Perovskite Materials. *Adv. Mater.* **2019**, *31*, 1805337.
- (11) Rajagopal, A.; Yao, K.; Jen, A. K. Y. Toward Perovskite Solar Cell Commercialization: A Perspective and Research Roadmap Based on Interfacial Engineering. *Adv. Mater.* **2018**, *30*, 1800455.

- (12) Tsai, H.; Nie, W.; Blancon, J.-C.; Toumpos, C. C. S.; Asadpour, R.; Harutyunyan, B.; Neukirch, A. J.; Verduzco, R.; Crochet, J. J.; Tretiak, S.; Pedesseau, L.; Even, J.; Alam, M. A.; Gupta, G.; Lou, J.; Ajayan, P. M.; Bedzyk, M. J.; Kanatzidis, M. G.; Mohite, A. D. High-Efficiency Two-Dimensional Ruddlesden-Popper Perovskite Solar Cells. *Nature* **2016**, *536*, 312–316.
- (13) Lai, H.; Kan, B.; Liu, T.; Zheng, N.; Xie, Z.; Zhou, T.; Wan, X.; Zhang, X.; Liu, Y.; Chen, Y. Two-Dimensional Ruddlesden-Popper Perovskite with Nanorod-Like Morphology for Solar Cells with Efficiency Exceeding 15%. *J. Am. Chem. Soc.* **2018**, *140*, 11639–11646.
- (14) Ren, H.; Yu, S. D.; Chao, L. F.; Xia, Y. D.; Sun, Y. H.; Zuo, S. W.; Li, F.; Niu, T. T.; Yang, Y. G.; Ju, H. X.; Li, B. X.; Du, H. Y.; Gao, X. Y.; Zhang, J.; Wang, J. P.; Zhang, L. J.; Chen, Y. H.; Huang, W. Efficient and Stable Ruddlesden-Popper Perovskite Solar Cell with Tailored Interlayer Molecular Interaction. *Nat. Photonics* **2020**, *14*, 154–163.
- (15) Li, X.; Ke, W.; Traore, B.; Guo, P.; Hadar, I.; Kepenekian, M.; Even, J.; Katan, C.; Stoumpos, C. C.; Schaller, R. D.; Kanatzidis, M. G. Two-Dimensional Dion-Jacobson Hybrid Lead Iodide Perovskites with Aromatic Diammonium Cations. *J. Am. Chem. Soc.* **2019**, *141*, 12880–12890.
- (16) Lu, D.; Lv, G. W.; Xu, Z. Y.; Dong, Y. X.; Ji, X. F.; Liu, Y. S. Thiophene-Based Two-Dimensional Dion-Jacobson Perovskite Solar Cells with over 15% Efficiency. *J. Am. Chem. Soc.* **2020**, *142*, 11114–11122.
- (17) Shi, E. Z.; Gao, Y.; Finkenauer, B. P.; Akriti; Coffey, A. H.; Dou, L. T. Two-Dimensional Dalide Perovskite Nanomaterials and Heterostructures. *Chem. Soc. Rev.* **2018**, *47*, 6046–6072.
- (18) Katan, C.; Mercier, N.; Even, J. Quantum and Dielectric Confinement Effects in Lower-Dimensional Hybrid Perovskite Semiconductors. *Chem. Rev.* **2019**, *119*, 3140–3192.
- (19) Grancini, G.; Nazeeruddin, M. K. Dimensional Tailoring of Hybrid Perovskites for Photovoltaics. *Nat. Rev. Mater.* **2019**, *4*, 4–22.
- (20) Zhang, F.; Lu, H. P.; Tong, J. H.; Berry, J. J.; Beard, M. C.; Zhu, K. Advances in Two-Dimensional Organic-Inorganic Hybrid Perovskites. *Energy Environ. Sci.* **2020**, *13*, 1154–1186.
- (21) Liu, Y. H.; Akin, S.; Pan, L. F.; Uchida, R.; Arora, N.; Milic, J. V.; Hinderhofer, A.; Schreiber, F.; Uhl, A. R.; Zakeeruddin, S. M.; Hagfeldt, A.; Dar, M. I.; Gratzel, M. Ultrahydrophobic 3D/2D Fluoroarene Bilayer-Based Water-Resistant Perovskite Solar Cells with Efficiencies Exceeding 22%. *Sci. Adv.* **2019**, *5*, No. eaaw2543.
- (22) Zhou, T.; Lai, H. T.; Liu, T. T.; Lu, D.; Wan, X. J.; Zhang, X. D.; Liu, Y. S.; Chen, Y. S. Highly Efficient and Stable Solar Cells Based on Crystalline Oriented 2D/3D Hybrid Perovskite. *Adv. Mater.* **2019**, *31*, 1901242.
- (23) Krishna, A.; Gottis, S.; Nazeeruddin, M. K.; Sauvage, F. Mixed Dimensional 2D/3D Hybrid Perovskite Absorbers: The Future of Perovskite Solar Cells? *Adv. Funct. Mater.* **2019**, *29*, 1806482.
- (24) Yao, Q.; Xue, Q. F.; Li, Z. C.; Zhang, K. C.; Zhang, T.; Li, N.; Yang, S. H.; Brabec, C. J.; Yip, H. L.; Cao, Y. Graded 2D/3D Perovskite Heterostructure for Efficient and Operationally Stable MA-Free Perovskite Solar Cells. *Adv. Mater.* **2020**, *32*, 2000571.
- (25) Proppe, A. H.; Wei, M. Y.; Chen, B.; Quintero-Bermudez, R.; Kelley, S. O.; Sargent, E. H. Photochemically Cross-Linked Quantum Well Ligands for 2D/3D Perovskite Photovoltaics with Improved Photovoltage and Stability. *J. Am. Chem. Soc.* **2019**, *141*, 14180–14189.
- (26) Li, P. W.; Zhang, Y. Q.; Liang, C.; Xing, G. C.; Liu, X. L.; Li, F. Y.; Liu, X. T.; Hu, X. T.; Shao, G. S.; Song, Y. L. Phase Pure 2D Perovskite for High-Performance 2D-3D Heterostructured Perovskite Solar Cells. *Adv. Mater.* **2018**, *30*, 1805323.
- (27) Wang, Z.; Lin, Q.; Chmiel, F. P.; Sakai, N.; Herz, L. M.; Snaith, H. J. Efficient Ambient-Air-Stable Solar Cells with 2D–3D Heterostructured Butylammonium-Caesium-Formamidinium Lead Halide Perovskites. *Nat. Energy* **2017**, *2*, 17135.
- (28) Zheng, X.; Deng, Y.; Chen, B.; Wei, H.; Xiao, X.; Fang, Y.; Lin, Y.; Yu, Z.; Liu, Y.; Wang, Q.; Huang, J. Dual Functions of Crystallization Control and Defect Passivation Enabled by Sulfonic Zwitterions for Stable and Efficient Perovskite Solar Cells. *Adv. Mater.* **2018**, *30*, No. e1803428.
- (29) Singh, T.; Miyasaka, T. Stabilizing the Efficiency beyond 20% with a Mixed Cation Perovskite Solar Cell Fabricated in Ambient Air under Controlled Humidity. *Adv. Energy Mater.* **2018**, *8*, 1700677.
- (30) Gharibzadeh, S.; Nejad, B. A.; Jakoby, M.; Abzieher, T.; Hauschild, D.; Moghadamzadeh, S.; Schwenzer, J. A.; Brenner, P.; Schmager, R.; Haghighirad, A. A.; Weinhardt, L.; Lemmer, U.; Richards, B. S.; Howard, I. A.; Paetzold, U. W. Record Open-Circuit Voltage Wide-Bandgap Perovskite Solar Cells Utilizing 2D/3D Perovskite Heterostructure. *Adv. Energy Mater.* **2019**, *9*, 1803699.
- (31) Pistor, P.; Greiner, D.; Kaufmann, C. A.; Brunken, S.; Gorgoi, M.; Steigert, A.; Calvet, W.; Lauermaun, I.; Klenk, R.; Unold, T.; Lux-Steiner, M. C. Experimental Indication for Band Gap Widening of Chalcopyrite Solar Cell Absorbers after Potassium Fluoride Treatment. *Appl. Phys. Lett.* **2014**, *105*, 063901.
- (32) Wu, X. X.; Trinh, M. T.; Niesner, D.; Zhu, H. M.; Norman, Z.; Owen, J. S.; Yaffe, O.; Kudisch, B. J.; Zhu, X. Y. Trap States in Lead Iodide Perovskites. *J. Am. Chem. Soc.* **2015**, *137*, 2089–2096.
- (33) Han, Q.; Bae, S. H.; Sun, P.; Hsieh, Y. T.; Yang, Y. M.; Rim, Y. S.; Zhao, H.; Chen, Q.; Shi, W.; Li, G.; Yang, Y. Single Crystal Formamidinium Lead Iodide (FAPbI₃): Insight into the Structural, Optical, and Electrical Properties. *Adv. Mater.* **2016**, *28*, 2253–2258.
- (34) Si, H. N.; Liao, Q. L.; Kang, Z.; Ou, Y.; Meng, J. J.; Liu, Y. C.; Zhang, Z.; Zhang, Y. Deciphering the NH₄PbI₃ Intermediate Phase for Simultaneous Improvement on Nucleation and Crystal Growth of Perovskite. *Adv. Funct. Mater.* **2017**, *27*, 1701804.
- (35) Li, X.; Dar, M. I.; Yi, C. Y.; Luo, J. S.; Tschumi, M.; Zakeeruddin, S. M.; Nazeeruddin, M. K.; Han, H. W.; Gratzel, M. Improved Performance and Stability of Perovskite Solar Cells by Crystal Crosslinking with Alkylphosphonic Acid Omega-Ammonium Chlorides. *Nat. Chem.* **2015**, *7*, 703–711.
- (36) Gallop, N. P.; Selig, O.; Giubertoni, G.; Bakker, H. J.; Rezus, Y. L. A.; Frost, J. M.; Jansen, T. L. C.; Lovrincic, R.; Bakulin, A. A. Rotational Cation Dynamics in Metal Halide Perovskites: Effect on Phonons and Material Properties. *J. Phys. Chem. Lett.* **2018**, *9*, 5987–5997.
- (37) Xu, Z. Y.; Lu, D.; Liu, F.; Lai, H. T.; Wan, X. J.; Zhang, X. D.; Liu, Y. S.; Chen, Y. S. Phase Distribution and Carrier Dynamics in Multiple-Ring Aromatic Spacer-Based Two-Dimensional Ruddlesden-Popper Perovskite Solar Cells. *ACS Nano* **2020**, *14*, 4871–4881.
- (38) Lu, J. F.; Jiang, L. C.; Li, W.; Li, F.; Pai, N. K.; Scully, A. D.; Tsai, C. M.; Bach, U.; Simonov, A. N.; Cheng, Y. B.; Spiccia, L. Diammonium and Monoammonium Mixed-Organic-Cation Perovskites for High Performance Solar Cells with Improved Stability. *Adv. Energy Mater.* **2017**, *7*, 1700444.
- (39) Saparov, B.; Mitzi, D. B. Organic-Inorganic Perovskites: Structural Versatility for Functional Materials Design. *Chem. Rev.* **2016**, *116*, 4558–4596.
- (40) Jodlowski, A. D.; Roldan-Carmona, C.; Grancini, G.; Salado, M.; Ralaifarisoa, M.; Ahmad, S.; Koch, N.; Camacho, L.; de Miguel, G.; Nazeeruddin, M. K. Large Guanidinium Cation Mixed with Methylammonium in Lead Iodide Perovskites for 19% Efficient Solar Cells. *Nat. Energy* **2017**, *2*, 972–979.
- (41) Wu, Z. F.; Raga, S. R.; Juarez-Perez, E. J.; Yao, X. Y.; Jiang, Y.; Ono, L. K.; Ning, Z. J.; Tian, H.; Qi, Y. B. Improved Efficiency and Stability of Perovskite Solar Cells Induced by C = O Functionalized Hydrophobic Ammonium-Based Additives. *Adv. Mater.* **2018**, *30*, 1703670.
- (42) Zhou, Y.; Wang, F.; Cao, Y.; Wang, J. P.; Fang, H. H.; Loi, M. A.; Zhao, N.; Wong, C. P. Benzylamine-Treated Wide-Bandgap Perovskite with High Thermal-Photostability and Photovoltaic Performance. *Adv. Energy Mater.* **2017**, *7*, 1701048.
- (43) Zhou, H.; Chen, Q.; Li, G.; Luo, S.; Song, T. B.; Duan, H. S.; Hong, Z.; You, J.; Liu, Y.; Yang, Y. Interface Engineering of Highly Efficient Perovskite Solar Cells. *Science* **2014**, *345*, 542–546.
- (44) Zhang, X.; Ren, X. D.; Liu, B.; Munir, R.; Zhu, X. J.; Yang, D.; Li, J. B.; Liu, Y. C.; Smilgies, D. M.; Li, R. P.; Yang, Z.; Niu, T. Q.; Wang, X. L.; Amassian, A.; Zhao, K.; Liu, S. Z. F. Stable High

Efficiency Two-Dimensional Perovskite Solar Cells via Cesium Doping. *Energy Environ. Sci.* **2017**, *10*, 2095–2102.

(45) Zhang, T. K.; Long, M. Z.; Qin, M. C.; Lu, X. H.; Chen, S.; Xie, F. Y.; Gong, L.; Chen, J.; Chu, M.; Miao, Q.; Chen, Z. F.; Xu, W. Y.; Liu, P. Y.; Xie, W. G.; Xu, J. B. Stable and Efficient 3D-2D Perovskite-Perovskite Planar Heterojunction Solar Cell without Organic Hole Transport Layer. *Joule* **2018**, *2*, 2706–2721.

(46) Dong, Q.; Fang, Y.; Shao, Y.; Mulligan, P.; Qiu, J.; Cao, L.; Huang, J. Electron-Hole Diffusion Lengths > 175 μm in Solution-Grown $\text{CH}_3\text{NH}_3\text{PbI}_3$ Single Crystals. *Science* **2015**, *347*, 967–970.

(47) Shi, D.; Adinolfi, V.; Comin, R.; Yuan, M. J.; Alarousu, E.; Buin, A.; Chen, Y.; Hoogland, S.; Rothenberger, A.; Katsiev, K.; Losovyj, Y.; Zhang, X.; Dowben, P. A.; Mohammed, O. F.; Sargent, E. H.; Bakr, O. M. Low Trap-State Density and Long Carrier Diffusion in Organolead Trihalide Perovskite Single Crystals. *Science* **2015**, *347*, 519–522.

(48) Lee, J. W.; Dai, Z.; Han, T. H.; Choi, C.; Chang, S. Y.; Lee, S. J.; De Marco, N.; Zhao, H.; Sun, P.; Huang, Y.; Yang, Y. 2D Perovskite Stabilized Phase-Pure Formamidinium Perovskite Solar Cells. *Nat. Commun.* **2018**, *9*, 3021.

(49) Wei, W. J.; Jiang, X. X.; Dong, L. Y.; Liu, W. W.; Han, X. B.; Qin, Y.; Li, K.; Li, W.; Lin, Z. S.; Bu, X. H.; Lu, P. X. Regulating Second-Harmonic Generation by van der Waals Interactions in Two-Dimensional Lead Halide Perovskite Nanosheets. *J. Am. Chem. Soc.* **2019**, *141*, 9134–9139.

(50) Chen, A. Z.; Shiu, M.; Ma, J. H.; Alpert, M. R.; Zhang, D. P.; Foley, B. J.; Smilgies, D. M.; Lee, S. H.; Choi, J. J. Origin of Vertical Orientation in Two-Dimensional Metal Halide Perovskites and Its Effect on Photovoltaic Performance. *Nat. Commun.* **2018**, *9*, 1336.

(51) Song, S.; Yang, S. J.; Choi, W.; Lee, H.; Sung, W.; Park, C.; Cho, K. Molecular Engineering of Organic Spacer Cations for Efficient and Stable Formamidinium Perovskite Solar Cell. *Adv. Energy Mater.* **2020**, *10*, 2001759.

(52) Zhang, C. L.; Wu, S. H.; Tao, L. M.; Arumugam, G. M.; Liu, C.; Wang, Z.; Zhu, S. S.; Yang, Y. Z.; Lin, J.; Liu, X. Y.; Schropp, R. E. I.; Mai, Y. H. Fabrication Strategy for Efficient 2D/3D Perovskite Solar Cells Enabled by Diffusion Passivation and Strain Compensation. *Adv. Energy Mater.* **2020**, *10*, 2002004.

(53) Liu, C.; Sun, J. S.; Tan, W. L.; Lu, J. F.; Gengenbach, T. R.; McNeill, C. R.; Ge, Z. Y.; Cheng, Y. B.; Bach, U. Alkali Cation Doping for Improving the Structural Stability of 2D Perovskite in 3D/2D PSCs. *Nano Lett.* **2020**, *20*, 1240–1251.

(54) Zhang, H.; Ren, X. G.; Chen, X. W.; Mao, J.; Cheng, J. Q.; Zhao, Y.; Liu, Y. H.; Milic, J.; Yin, W. J.; Gratzel, M.; Choy, W. C. H. Improving the Stability and Performance of Perovskite Solar Cells via Off-the-Shelf Post-Device Ligand Treatment. *Energy Environ. Sci.* **2018**, *11*, 2253–2262.